A Neural Network-Enabled OTFS-PAPR Reduction with Low Computational Complexity

Mohammed I. AL-RAYIF, Eldaw E. ELDUKHRI

Dept. of Applied of Electrical Engineering, College of Applied Engineering, King Saud University, Almuzahmia Branch,
P.O. Box 800, 11421 Riyadh City, Saudi Arabia

malrayif@ksu.edu.sa, eeldukhri@ksu.edu.sa

Submitted October 2, 2025 / Accepted December 14, 2025 / Online first January 26, 2026

Abstract. *This study proposes a new solution to overcome the high peak-to-average power ratio (PAPR) in Orthogonal Time Frequency Space (OTFS) by using an Artificial Neural Network (ANN) algorithm. The algorithm checks the magnitude (power) of each element in the matrix of the first stage of the inverse symplectic finite Fourier transform (ISFFT) process against a pre-specified threshold and, consequently adjusts the elements whose magnitudes exceed the threshold. This is achieved by using the ANN algorithm to apply fractional shifts to the elements of the original delay-Doppler (DD) data matrix without changing their orientation. The simulation results demonstrated a significant PAPR reduction while maintaining the system performance in terms of the Bit Error Rate (BER), with almost the same computational complexity of the conventional OTFS system.*

Keywords

OTFS, PAPR, ISFFT, artificial neural networks

1. Introduction

Orthogonal time frequency space (OTFS) is an attractive system which provides a significant improvement in the transmission quality of a high Doppler environment, and one of the possible future 6G communication technologies [1]. However, as any other multicarrier technique, OTFS suffers from the high peak-to-average power ratio (PAPR) due to the unpredictable matching of baseband signals' phases during the operations of transformation from delay-Doppler (DD) domain to time-frequency (TF) domain, i.e., the operation of inverse symplectic finite Fourier transform (ISFFT) [1], [2]. The components with high peaks will be clipped when passing through the non-linear power amplifier (NLPA), where the saturation level is the edge of NLPA linearity, causing a distorted waveform. In other words, the clipped signal will introduce an out-of-band radiation and in-band distortion, which, in return, will decay system performance [1–3]. Consequentially, several studies on various aspects of PAPR reduction have been conducted to overcome this challenge. It is possible to, broadly, classify these studies into four categories; namely: distortionless schemes (e.g., selective mapping (SLM) and partial transmit sequence (PTS)) [4], [5]; clipping and filtering [6], [7]; encoding schemes [8], [9]; and artificial intelligence networks (ANN) enabled methods [10], [11]. Each of these approaches needs a trade off between PAPR reduction, system performance and computational complexity. This work is related to the ANN-enabled category for PAPR reduction, hence we will focus our analysis on recent works presented under this category. In [12], the PAPR reduction method based on the autoencoder (AE) architecture through deep learning (DL) techniques was presented, where the encoder was designed to reduce the PAPR while the decoder was trained to reconstruct the original signal. This work needed a recovery process at the receiver, resulting in, an additional computational complexity. In [10], an automatic amplitude reduction neural network algorithm was proposed. The algorithm was combined with PTS and SLM methods using the Vendermonde matrix for generating phase sequences, to reduce complexity when selecting the optimal phase. Moreover, a particle swarm optimization (PSO) algorithm was used with sub-optimal PTS/SLM in [13]. Although, both approaches showed significant PAPR reduction results, the BER showed unreasonable performance levels indicating that the OTFS with PAPR reduction performed better than the original OTFS frame. Also, there were very limited details about the construction and recovery process of the proposed schemes. For instance, the parameters of OTFS channel, power amplifier, detectors, SLM/PTS recovery, etc., were not provided. Also, an OFSM-PAPR reduction scheme based on random-SLM and orthogonal-SLM was proposed in [14]. Even though it showed reasonable results in terms of CCDF-PAPR and BER, it suffered from the overall high computational complexity where its detectors needed to be modified to introduce the transmitted side information of SLM used at the transmitter.

To the best of the authors' knowledge, there was no previous study that addressed the subject of OTFS-PAPR reduction using ANN technique as proposed in this paper, except the work related to OFDM-PAPR reduction reported in [3] which used similar ANN approach.

DOI: 10.13164/re.2026.0105

In this paper, the proposed ANN scheme is applied to reduce the PAPR in OTFS system while maintaining reasonable BER performance levels. Here, the first transformation process of the ISFFT (i.e., IFFT$[\cdot]$) is considered for power peaks measurement for each element of the IFFT output matrix. The element with the peak that exceeds the given threshold (usually the saturation level of the NLPA) is adjusted via the ANN process which reduces the particular peak by shifting the elements of the original delay-Doppler (DD) matrix fractionally. This modification leads to reducing the PAPR while maintaining the system performance (BER). In addition, no recovery process is required at the receiver, as neither side information for PAPR reduction is transmitted nor high modification is applied to the original data phases/magnitudes. Consequently, no significant additional computational complexity is required with this scheme as the proposed ANN algorithm only operates when the magnitude of an element of the IFFT matrix exceeds the given threshold.

The main contributions of this study include:

- The concept of artificial neural networks (ANN) was implemented to maintain the power peaks of an OTFS system within a certain threshold. This was achieved by considering only the first matrix of the ISFFT process for identifying peaks which exceed the threshold. Consequently, the proposed approach attained satisfactory performance targets with low level of computational complexity when compared to techniques based on, for example, deep learning.
- The proposed ANN scheme satisfied a reasonable OTFS-PAPR reduction while maintaining an acceptable system BER performance, in the presence of a multi-fading channel.
- Unlike the conventional techniques (such as clipping, SLM/PTS, etc.), the proposed ANN technique did not require transmission of side information for a recovery process at the receiver. As a result, the original OTFS detectors (without any modification) can be used to detect the transmitted information, making the computational complexity of the proposed scheme almost equivalent to that of the conventional OTFS system.

The rest of the paper is organized as follows. In Sec. 2, the OTSM system model together with the proposed ANN scheme for PAPR reduction are presented. Simulation results and discussions are given in Sec. 3. Finally, concluding remarks are provided in Sec. 4.

2. System Model

Assume that the OTFS system operates on a P-path of channel with a bandwidth B, maximum delay spread $\tau_{\max}$, and maximum Doppler shift $\nu_{\max}$. The equivalent discrete-time baseband model is obtained by sampling the continuous-time OTFS signal at a sampling frequency $f_s = B = 1/T_s$, where T_s denotes the sampling interval. The discrete-time domain OTFS frame contains NM samples subdivided into N blocks, with M samples per block, as shown in Fig. 1. Hence, the OTFS frame duration is $T_f = NT$ where $T = MT_s$ which denotes the duration of each block. Consequently, every T seconds, the discrete spectrum of each block is obtained resulting from an M-point discrete Fourier transform (DFT), where the spectrum samples are spaced by $\Delta f = 1/T$. By collecting all N spectra of bandwidth $B = M\Delta f$ along the time axis defines the discrete time-frequency domain, as shown in Fig. 1, [15–17]. It is worth mentioning that the main source of PAPR rise in any multicarrier technique (say OFDM, OTFS, OTSM, etc.) is the length/size of the

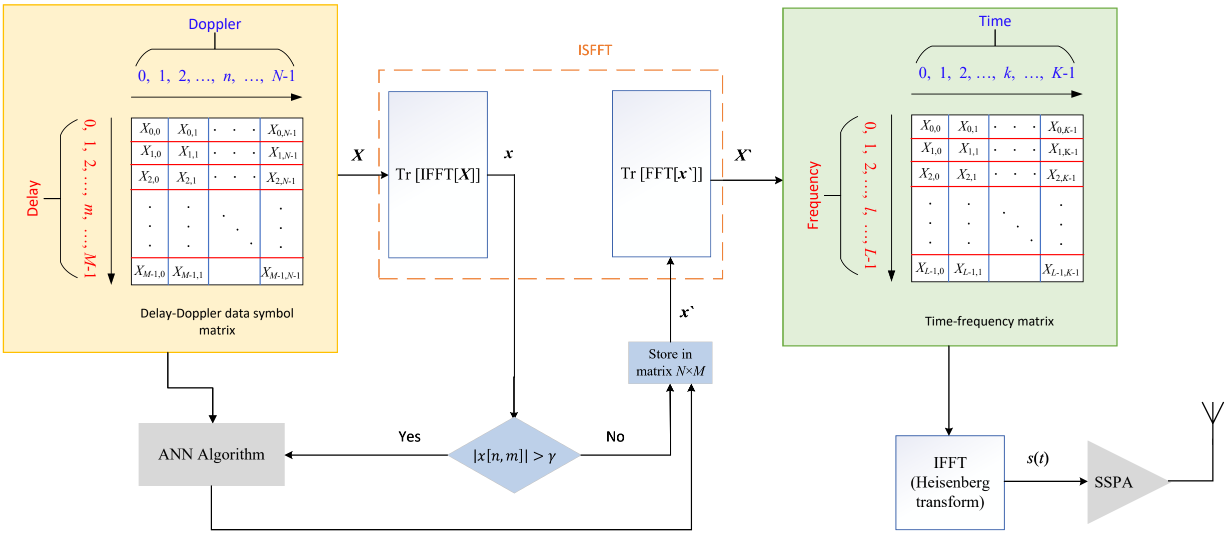

Fig. 1. Block diagram of OTFS with the proposed ANN-PAPR reduction.

sub carrier itself. Hence, with an increased size ($N \times M$) of the OTFS matrix, the PAPR will increase dramatically, regardless of use of a pilot scheme during the process. Of course, using the pilot scheme will make the situation worse but not as much as the size of the OTFS matrix. Therefore, with the emphasis on dimensionality, this work is focused on studying PAPR in a multicarrier OTFS system without use of a pilot scheme.

2.1 Principle of OTFS

In this section, the principle of OFTS will be explained using relevant information presented in [15–18]. Denote the transmitted and received blocks as $\mathbf{X}$ and $\mathbf{Y}$, respectively. Consider that both blocks are two-dimensional (2D) which indicate symbols of delay-Doppler (DD) matrix, i.e. $\mathbf{X}, \mathbf{Y} \in M \times N$, with $\mathbf{x}_m$ and $\mathbf{y}_m$ be the symbol vectors in the m-th row, where $\mathbf{x}_m = \left[X(m,0), X(m,1), \ldots, X(m,N-1)\right]^{\mathrm{T}}$ and $\mathbf{y}_m = \left[Y(m,0), Y(m,1), \ldots, Y(m,N-1)\right]^{\mathrm{T}}$, given that $m = 0, 1, \ldots, M-1$ and $n = 0, 1, \ldots, N-1$ denote the delay and Doppler indices respectively. Based on the principle of OTFS, the DD information symbol matrix $\mathbf{X}$ is generated from a certain QAM alphabet $\mathbb{A} = \left\{a_1, \ldots, a_Q\right\}$ of size Q, i.e., $\mathbf{X} \in \mathbb{C}^{M \times N}$. Hence, to transfer this matrix to time-frequency matrix $\mathbf{X}_{\mathrm{tf}}$, the inverse symplectic fast Fourier transform (ISFFT) process is applied as follows:

$$\mathbf{X}_{\mathrm{tf}}[l,k] = \frac{1}{\sqrt{MN}} \sum_{n=0}^{N-1} \sum_{m=0}^{M-1} \mathbf{X}[m,n]\, \mathrm{e}^{\mathrm{j}2\pi\left\{\frac{nk}{N} - \frac{ml}{M}\right)} \tag{1}$$

for $l = 0, 1, \ldots, M-1$ and $k = 0, 1, \ldots, N-1$, where $\mathbf{X}_{\mathrm{tf}} \in \mathbb{C}^{M \times N}$. Next, this matrix $\mathbf{X}_{\mathrm{tf}}$ is converted to 1D continuous-time waveform $s(t)$ using a transmit waveform $g_{\mathrm{tx}}(t)$ as:

$$s(t) = \sum_{k=0}^{N-1} \sum_{l=0}^{M-1} \mathbf{X}_{\mathrm{tf}}[l,k]\, g_{\mathrm{tx}}(t - kT)\, \mathrm{e}^{\mathrm{j}2\pi l \Delta f (t-kT)}. \tag{2}$$

Notice that for rectangular waveform, $\mathbf{G}_{\mathrm{tx}} = \operatorname{diag}\left[g_{\mathrm{tx}}(0), g_{\mathrm{tx}}(T/M), \ldots, g_{\mathrm{tx}}(((M-1)T/M)\right] \in \mathbb{C}^{M \times M}$ reduces to the identity matrix $\mathbf{I}_M$, and $\mathbf{S} = \mathrm{IFFT}\left[\mathbf{X}_{\mathrm{tf}}^{\mathrm{T}}\right]$ in matrix form. This is followed by the row-wise vectorization to obtain the time domain samples vector with length of $NM \times 1$ as [15]:

$$\mathbf{s} = \operatorname{vec}(\mathbf{S}) \in \mathbb{C}^{MN \times 1}. \tag{3}$$

Next, the cyclic prefix (CP) is added to the tail of $\mathbf{s}$ with the length $\geq l_{\max}$, where $l_{\max}$ is the maximum channel delay spread. Consider a baseband equivalent channel model with P propagation paths. For the i-th path, $i = 0, 1, \ldots, P-1$, the complex path gain is g_i, and the actual delay and Doppler shift are $\tau_i = \frac{l_i}{M\Delta f}$ and $\nu_i = \frac{\kappa_i}{NT}$, respectively, where $\tau_i \leq \tau_{\max} = \frac{l_{\max}}{M\Delta f}$ and $\mid \nu_i \mid \leq \nu_{\max}$, $l_i, \kappa_i \in \mathbb{R}$ are the normalized delay and normalized Doppler shift, respectively, and $l_{\max} \in \mathbb{R}$ is the normalized delay associated with $\tau_{\max}$ [15–17]. Considering that the channel is under-spread, i.e., $\tau_{\max}\nu_{\max} \ll 1$ and $T\Delta f = 1$, the received signal $r(t)$, after transmitting $s(t)$ over a time-varying channel with delay-Doppler channel response $h(\tau, \nu)$, is given as:

$$r(t) = \int g(\tau, t)\, s(t - \tau)\, \mathrm{d}\tau + \omega(t) \tag{4}$$

where $g(\tau, t) = \int_{\nu} h(\tau, \nu)\, \mathrm{e}^{\mathrm{j}2\pi\nu(t-\tau)} \mathrm{d}\nu$ is the delay-time response, with $h(\tau, \nu) = \sum_{p=1}^{P} h_p \delta\left(\tau - \tau_p\right) \delta\left(\nu - \nu_p\right)$, and $\omega(t)$ is independent and identically distributed additive white Gaussian noise (iid AWGN) with zero mean and variance σ_{ω}^2. After removing the cyclic prefix and by sampling the received signal at a rate $f_{\mathrm{s}} = M/T = M\Delta f$, the vector $\mathbf{r} = \{r(n)\}_{n=0}^{NM-1}$ is formed as:

$$\mathbf{r} = \mathbf{H}\mathbf{s} + \mathbf{w} \tag{5}$$

where $\mathbf{H} \in \mathbb{C}^{MN \times MN}$ is the channel matrix as formulated in [15], [18]. The vector $\mathbf{r}_n \in \mathbb{C}^{M \times 1}$, for $n = 0, 1, \ldots, N-1$ is converted to the delay-time matrix $\tilde{\mathbf{Y}} \in \mathbb{C}^{M \times N}$ as:

$$\tilde{\mathbf{Y}} = \mathbf{G}_{\mathrm{rx}} \cdot \left(\operatorname{vec}_{M,N}^{-1}(\mathbf{r})\right) \tag{6}$$

where $\operatorname{vec}_{M,N}^{-1}(\mathbf{r})$ is the operation to convert $\mathbf{r}_n$ to the matrix $M \times N$, and the diagonal matrix $\mathbf{G}_{\mathrm{rx}}$ is the receiver pulse shaping matrix, considering that $\mathbf{G}_{\mathrm{rx}} = \mathbf{I}_M$ for rectangular pulse shaping waveforms, i.e., $\tilde{\mathbf{Y}} = \operatorname{vec}_{M,N}^{-1}(\mathbf{r})$. Next, the time-frequency transform is performed as $\mathbf{Y}_{\mathrm{tf}} \in \mathbb{M} \times \mathbb{N}$ received samples matrix, by applying M-points DFT operation on the delay-time samples, hence $\mathbf{Y}_{\mathrm{tf}} = \mathbf{F}_M \cdot \tilde{\mathbf{Y}}$. These operations is known as Wigner transform [15], [17]. To get back to the delay-Doppler domain, an SFFT operation is performed. Hence, operations of SFFT and Wigner transform can be simplified as:

$$\mathbf{Y} = \mathbf{F}_M^{\mathrm{H}} \cdot \mathbf{Y}_{\mathrm{tf}} \cdot \mathbf{F}_N = \tilde{\mathbf{Y}} \cdot \mathbf{F}_N. \tag{7}$$

For the detection process, two multipath channel model detectors; namely: Message Passing (MP) detector and Maximum-Ratio Combining (MRC) detector have been implemented with the assumption that their channel state information is known to the receiver. While the MP detector is considered for the channel model of L-taps with unform power, the MRC detector is considered for the multipath fading channel of EVA model at a high speed user. Both models were represented in [15]. Hence, for the MP scenario, given that the OTFS input-output relation $\mathbf{y} = \mathbf{H} \cdot \mathbf{x} + \mathbf{z}$, where $\mathbf{y} = \operatorname{vec}\left(\mathbf{Y}^{\mathrm{T}}\right)$, $\mathbf{x} = \operatorname{vec}\left(\mathbf{X}^{\mathrm{T}}\right)$ are the corresponding samples vectors, with $\mathbf{x}, \mathbf{y} \in \mathbb{C}^{NM \times 1}$. Accordingly, a NM variable nodes corresponding to $\mathbf{x}$ and NM observation nodes corresponding to $\mathbf{y}$ is considered as the MP system model. After some analysis steps, based on [15], [16], the MP detection can be expressed as:

$$\hat{x}[c] = \arg\max_{a_j \in \mathbb{A}} \left(p_c^{(i)}\left(a_j\right)\right), c = 0, 1, \ldots, NM-1 \tag{8}$$

where $\hat{x}[\cdot]$ is the estimated information element, $\mathbb{A} = \left\{a_1, a_2, \ldots, a_Q\right\}$ represents a modulation alphabet of size Q, and $p_c^{(i)}\left(a_j\right)$ is the probability mass function (pmf) of the alphabet corresponds to the message passed from a variable node $x[c]$ to the observation nodes $y[d]$ (as expressed in (9)). Let $\mathcal{I}(d)$ and $\mathcal{J}(c)$ denote the sets of indeces with nonzero elements in the d-th row and c-th column, respectively, with $c, d = 0, 1, \ldots, NM - 1$ and $d \in \mathcal{J}(c)$, the pmf can be expressed as:

$$p_c^{(i)}\left(a_j\right) = \prod_{e\in\mathcal{J}(c)} \frac{\xi^{(i)}\left(e,c,j\right)}{\sum_{k=1}^{Q}\xi^{(i)}\left(e,c,k\right)} \tag{9}$$

where $\xi_{d,c}^{(i)}$ represents the approximate Gaussian random variable, associated with i-th iteration, of the mean $\mu_{d,c}^{(i)}$ and variance $\left(\sigma_{d,c}^{(i)}\right)^2$ of the interference $\sum_{e\in\mathcal{I}(d),e\neq c} x[e]H[d,e] + z[d]$. For the second scenario, that is MRC detector with EVA channel mode, after removing the cyclic prefix components, recalling the transmitted and received subvectors (along the Doppler domain) $\mathbf{x}_m, \mathbf{y}_m \in \mathbb{C}^{N\times 1}$, respectively, for $m = 0, 1, \ldots, M-1$, the matrix channel $\mathbf{H}$ contains submatrices $\mathbf{K}_{m,l} \in \mathbb{C}^{N\times N}$ representing the linear-time variant channel between the m-th received block and the $[m-l]_M$-th transmitted block for $l \in \mathcal{L}$, where $\mathcal{L}$ is the set of the distinct normalized delay shifts of the channel. Hence, the received samples can be expressed as: $\mathbf{y}_m = \sum_{l\in\mathcal{L}} \mathbf{K}_{m,l}\cdot\mathbf{x}_{[m-l]_M} + \mathbf{z}_m$ where $\mathbf{z}_m \in \mathbb{C}^{N\times 1}$ is the AWGN noise and $\mathbf{x}_{[m-l]_M}$ can be reduced to $\mathbf{x}_{m-l}$ after removing the cyclic prefix. Let $\mathbf{b}_m^l \in \mathbb{C}^{N\times 1}$ be the channel impaired signal component of $\mathbf{x}_m$ in the received vectors $\mathbf{y}_{m+l}$ after removing the interference of other transmitted symbol vectors $\mathbf{x}_k$ for $k \neq m$. Thus, under assumption that the $\mathbf{x}_m$ was estimated from the previous iteration, $\mathbf{b}_m^l$ can be expressed as:

$$\mathbf{b}_m^l = \mathbf{y}_{m+l} - \underbrace{\sum_{l'\in\mathcal{L},l'\neq l} \mathbf{K}_{m+l,l'}\cdot\widehat{\mathbf{x}}_{m+l-l'}}_{\text{inter-delay-interference}} \tag{10}$$

where $\widehat{\mathbf{x}}_{m+l-l'} = \mathbf{0}$ for $m+l-l' < 0$, $0 \leq l' \leq l_{\max}$ and $\mathbf{K}_{m+l,l'}$ are the submatrices of the extended delay-Doppler channel matrix $\mathbf{H}$. Given that $\mathbf{y}_{m'} = \sum_{l'\in\mathcal{L}} \mathbf{K}_{m',l'}\cdot\mathbf{x}_{m'-l'} + \mathbf{z}_{m'}$ with $m' = m + l$ and by substituting this expression into (10), it yields:

$$\mathbf{b}_m^l = \mathbf{K}_{m+l,l}\cdot\mathbf{x}_m + \underbrace{\sum_{l'\in\mathcal{L},l'\neq l} \mathbf{K}_{m+l,l'}\cdot\left(\mathbf{x}_{m+l-l'} - \widehat{\mathbf{x}}_{m+l-l'}\right) + \mathbf{z}_{m+l}}_{\text{interference and noise}}\,. \tag{11}$$

Performing maximal ratio combining of the channel impaired components $\mathbf{b}_m^l$ results in:

$$\mathbf{c}_m = \left(\sum_{l\in\mathcal{L}} \mathbf{K}_{m+l,l}^{\dagger}\cdot\mathbf{K}_{m+l,l}\right)^{-1}\cdot\left(\sum_{l\in\mathcal{L}} \mathbf{K}_{m+l,l}^{\dagger}\cdot\mathbf{b}_m^l\right) = \mathbf{D}_m^{-1}\cdot\mathbf{g}_m \tag{12}$$

where $\mathbf{c}_m \in \mathbb{C}^{N\times 1}$ is the vector output of the maximal ratio combiner, $\mathbf{D}_m = \sum_{l\in\mathcal{L}} \mathbf{K}_{m+l,l}^{\dagger}\cdot\mathbf{K}_{m+l,l}$ and $\mathbf{g}_m = \sum_{l\in\mathcal{L}} \mathbf{K}_{m+l,l}^{\dagger}\cdot\mathbf{b}_m^l$. The symbol-by-symbol maximum likelihood detection (MLD) is implemented resulting in the hard estimates given by:

$$\widehat{\mathbf{x}}_m\left[n\right] = \underbrace{\arg\min}_{a_j\in Q} \left|a_j - \mathbf{c}_m\left[n\right]\right| \tag{13}$$

where a_j is a signal from the QAM alphabet $\mathbb{A}$ of size Q with $j = 1, 2, \ldots, Q$ and $n = 0, 1, \ldots, N-1$. Once $\widehat{\mathbf{x}}_m$ is updated, m is increased and the same procedure is repeated to estimate all M symbol vectors $\widehat{\mathbf{x}}_m$.

2.2 Proposed ANN Scheme for OTFS-based PAPR Reduction

It is well known that the PAPR reduction process is implemented, mainly, at the transmitter, hence, it is pertinent first to introduce the proposed artificial neural network (ANN) scheme for PAPR reduction, herein referred to as ANN-PAPR. The key characteristic of the proposed scheme, which distinguishes it from most of the traditional PAPR reduction techniques, is its ability to modify the delay-Doppler information matrix in a manner that maintains the orientation of its elements, eliminating the need for a recovery process at the receiver. This, in turn, removes the computational complexity associated with the recovery process [3]. For implementing the ANN-PAPR scheme, a backpropagation learning method is utilized on a single-neuron, feedforward ANN model with multiple inputs, a sigmoid activation function and a single output [19].

From Fig. 1, each complex symbol in the information symbol matrix $\mathbf{X} \in \mathbb{C}^{M\times N}$, in the delay-Doppler domain, is obtained from a modulation alphabet $\mathbb{A} = \left\{a_1, a_2, \ldots, a_Q\right\}$. By applying the first stage of ISFFT process which takes an M-point DFT of the columns of $\mathbf{X}$, the transformed $\mathbf{x}$ matrix is obtained. Next, the magnitude of each element of $\mathbf{x}$, i.e., $|x(n,m)|$, is computed and compared to a given threshold γ, $(\gamma = \epsilon A_0)$, where $0 < \epsilon < 1$ is for controlling the threshold level and A_0 is the saturation level of a certain non-linear power amplifier. If $|x(n,m)| \leq \gamma$, the ANN-PAPR reduction scheme is not implemented and the element $x(n,m)$ is stored at its corresponding location in a new matrix $\mathbf{x}'$. On the other hand, if $|x(n,m)| > \gamma$, then this particular element $x(n,m)$ is adjusted to $x'(n,m)$ via the ANN-PAPR reduction scheme by modifying the elements of the original delay-Doppler matrix $\mathbf{X}$, that is $X(m,n)$ for $m = [0, 1, \ldots, M-1]$ and $n = [0, 1, \ldots, N-1]$ until the threshold condition is satisfied, i.e., $|x'(n,m)| \leq \gamma$.

It is worth noting that during our study of ISFFT behavior, we found that the resulting matrix $\mathbf{x}$ of the M-DFT transformation is equivalent to the Heisenberg output transform matrix $\mathbf{S} \in \mathbb{C}^{M\times N}$. In other words, variations in the elements of $\mathbf{S}$ are directly linked to variations in their counterparts in $\mathbf{x}$. Therefore, and without loss of generality, we utilized this feature and based our study on applying the proposed ANN-PAPR scheme to adjust the elements of the matrix $\mathbf{X}$ whose magnitudes in the matrix $\mathbf{x}$ exceed the specified threshold.

Figure 2 depicts the ANN model used and its components for performing the desired adjustments. To derive the ANN model, let the error $\Gamma = |\gamma - |x(n,m)||$ represents the difference between the threshold and magnitude of $|x(n,m)|$ and η denotes the ANN learning rate (set to 0.5 in this study

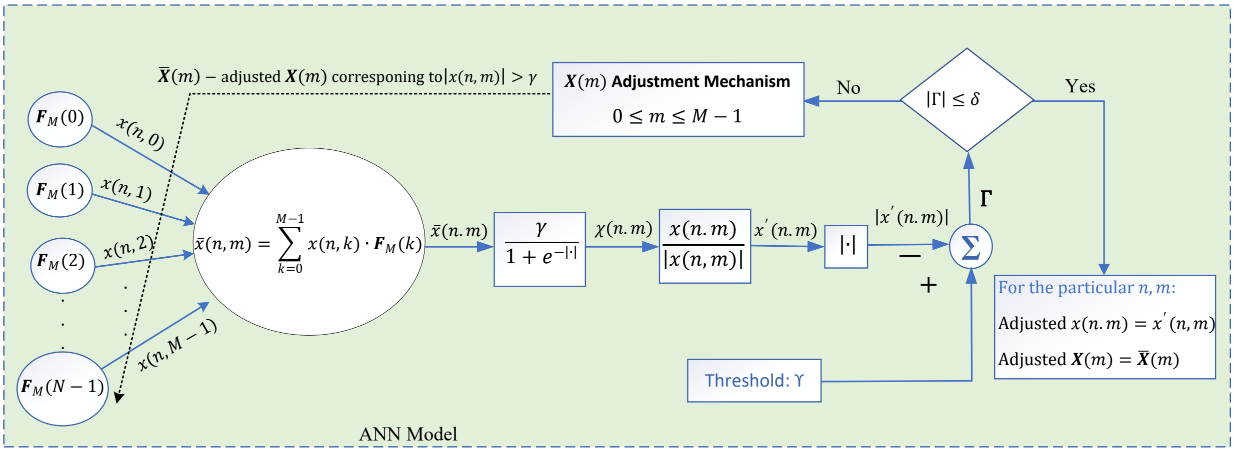

Fig. 2. Block diagram of the proposed ANN scheme.

without prejudicing other values in the range). Then the incremental change Δ_x in the transform $\mathbf{x}$ is obtained using the M-DFT transform matrix $\mathbf{F}_M$ as follows [3]:

$$\Delta_x = \eta \cdot \Gamma \cdot \mathbf{F}_M. \tag{14}$$

Consequently, the original Delay-Data matrix is updated to $\bar{\mathbf{x}} = \mathbf{x} + \Delta_x$ and the modified transformed element is expressed as:

$$\bar{x}(n,m) = [\bar{\mathbf{x}}(m) \cdot \mathbf{F}_M(n)]^{\mathrm{T}} \tag{15}$$

where, $\bar{\mathbf{x}}(m) = \begin{bmatrix} x(n,0) \\ x(n,1) \\ \vdots \\ x(n,M-1) \end{bmatrix}$, $\mathbf{F}_M(n) = \begin{bmatrix} \mathrm{e}^{\frac{-\mathrm{j}2\pi(0)m}{N}} \\ \mathrm{e}^{\frac{-\mathrm{j}2\pi(1)m}{N}} \\ \vdots \\ \mathrm{e}^{\frac{-\mathrm{j}2\pi(N-1)m}{N}} \end{bmatrix}$.

Next, the magnitude of the adjusted element is checked against the threshold γ as follows:

$$\mathcal{X}(n,m) = \frac{\gamma}{1+\mathrm{e}^{-|\bar{x}(n,m)|}}. \tag{16}$$

Finally, to maintain its original orientation, the adjusted element is modified and stored in its corresponding location inside the transformed matrix $\mathbf{x}'$ as:

$$x'(n,m) = \frac{\mathcal{X}(n,m)x(n,m)}{|x(n,m)|}. \tag{17}$$

This process is iterated until the condition is satisfied, that is $|x'(n,m)| \leq \gamma$ or the error $\Gamma = |\gamma - |x(n,m)|| = \delta$ is a tolerable error margin ($\delta = 0.005$ in this study as stopping criterion). Algorithm 1 lists the steps required to implement the ANN model. After adjusting all the elements of $\mathbf{x}$ whose magnitudes exceeded the specified threshold γ, the second stage of the ISFFT transform will be performed to obtain the Heisenberg transform as the final output.

Algorithm 1. Proposed ANN algorithm pseudocode.

```
INITIALIZE: $M, N, \mathbf{X}, \mathbf{F}_M, \gamma, \eta, \delta$.
REMARK: $\alpha \in \{n : 0, \dots, N-1\}, \beta \in \{m : 0, \dots, M-1\}$.
  for $n = 0 : N-1$   [Delay dimension]
    for $m = 0 : M-1$   [Doppler dimension]
      if $|x(n,m)| > \gamma \rightarrow x(\alpha,\beta) = x(n,m)$ , $\Gamma$ , $i = 1$.
        $\Gamma = |\gamma - |x(\alpha,\beta)||$
      while $|\Gamma| > \delta$ & $i$ = max. iter.
        $\Delta_x = \eta \cdot \Gamma \cdot \mathbf{F}_M$   [Eq. (14)]
        $\bar{\mathbf{x}} = \mathbf{x} + \Delta_x$
        $\bar{x}(\alpha,\beta) = [\bar{\mathbf{x}}(m) \cdot \mathbf{F}_M(n)]^{\mathrm{T}}$   [Eq. (15)]
        $\mathcal{X}(\alpha,\beta) = \frac{\gamma}{1+\mathrm{e}^{|\bar{x}(\alpha,\beta)|}}$   [Eq. (16)]
        $x'(\alpha,\beta) = \frac{\mathcal{X}(\alpha,\beta)x(n,m)}{|x(n,m)|}$   [Eq. (17)]
        $\Gamma = |\gamma - |x'(\alpha,\beta)||$
        $i = i + 1$
      end while
      end if
    end for
  end for
OUTPUT: $(x'(\alpha,\beta))$.
```

The PAPR performance is studied by considering the well-known Complementary Cumulative Distribution function of PAPR (CCDF-PAPR) (with a rectangular pulse shape) which is computed at the output of Heisenberg operation $\mathbf{s} \in \mathbb{C}^{NM\times 1}$ as [15], [20]:

$$P\left(\mathrm{PAPR} > \mu_0\right) = 1 - \left(1 - \mathrm{e}^{-\mu_0}\right)^{MN} \tag{18}$$

where $P\left(\mathrm{PAPR} > \mu_0\right)$ is the probability that the PAPR exceeds a given threshold μ_0 (which is abbreviated in some literature as PAPR_0) and the PAPR is calculated as

$$\mathrm{PAPR} = \frac{\max\limits_n \left\{|s\left(n\right)|^2\right\}}{\mathrm{E}\left\{|s\left(n\right)|^2\right\}}, \tag{19}$$

where $\mathrm{E}\{\cdot\}$ is the expectation operation, i.e., the average power of the transmitted OTFS frame $\mathbf{s}$. Notice that the theoretical CCDF-based SLM-PAPR reduction technique is expressed as $\left(1-(1-\mathrm{e}^{-\mu_0})^{MN}\right)^{U}$. Finally, the OTFS frame is transmitted through the physical channel after passing through the non-linear power amplifier (NLPA). In this study, the NLPA Solid-State power amplifier (SSPA) is considered, Rapp model [21], [22]. This kind of power amplifier ignores the effect of phase modification, hence only the amplitude of the input signal is amplified with the following expression:

$$\mathcal{A}\left[|\mathbf{s}|\right]=\frac{K_1|\mathbf{s}|}{\left[1+\left(\frac{K_1|\mathbf{s}|}{A_0}\right)^{2\rho}\right]^{\frac{1}{2\rho}}} \tag{20}$$

where $A_0=\sqrt{\mathrm{IBO}\cdot E\left\{\mathbf{s}\right\}}$ is the saturating amplitude at a specific *input-back-off* (IBO), K_1 (ignored in this study) is the small signal gain, ρ (set to 3 in this study) is a parameter which controls the smoothness of the transition from the linear region to the saturation region . Notice that, at the receiver, no further operation is needed, where the message point (MP) detector is applied after CP removal and SFFT operation as explained in the previous section.

2.3 Computational Complexity

As the proposed ANN-PAPR reduction scheme is applied at the transmitter, it is relevant to consider the computational complexity for the OTFS modulation in conjunction with the proposed ANN-PAPR scheme, in addition to the computational complexity of SLM scheme at the transmitter. Notice that, a specific operation is not required at the receiver to detect the ANN-based OTFS signal, which means that the same MP or MRC detector of the conventional OTFS is used for the proposed signal detection, and, as a result, the computational complexity of the conventional OTFS detector is maintained, i.e., $O\left(\mathrm{n_{iter}}NMSQ\right)$ for MP detector with S set of observation nodes, and $O\left(M\left(N^3+\mathrm{n_{iter}}N^2|\mathcal{L}|\right)\right)$ for MRC detector where $\mathrm{n_{iter}}$ is the number of detector's iteration and $\mathcal{L}$ is the set of the distinct normalized delay shifts of the channel [15]. Unlike in other techniques, say SLM and PTS scheme, where it needs a spatial detector (depending on the suggested SLM/PTS scheme) for side information recovery, which increases the computational complexity. Therefore, comparisons of computational complexity at the transmitter only is considered as discussed below for the proposed ANN-based OTFS, conventional OTFS, and SLM-OTFS systems.

Referring to [15] and [23], the following discussions are provided. The original OTFS complexity in terms of the respective number of complex multiplications (CMs) is equivalent to $\left(MN\log_2(M)+\frac{MN}{2}\log_2(N)\right)$. Additionally, the complexity produced by the proposed ANN-PAPR scheme can be observed, mainly, in (15) and in the operation of the ANN algorithm (Algorithm 1) with the maximum iterations equals to $\mathcal{I}_{\mathrm{iter}}$. Particularly, Equation (15) shows CMs equal to $\left(\frac{M}{2}\log_2(M)\right)$ where the operation is vectorizal applied, simultaneously, for vectors M and N, i.e. the same as OFDM frame operation with $M=N$. The resulting complexity order of iteration is $O(\mathcal{I}_{\mathrm{iter}})$. Consequently, the overall complexity order of the proposed OTFS is $\left(\frac{2N+1}{2}\right)M\log_2(M)+\mathcal{I}_{\mathrm{iter}}\left(\frac{MN}{2}\log_2(N)\right)+O(\mathcal{I}_{\mathrm{iter}})$. It is worth mentioning here that the proposed ANN-PAPR scheme only operates for a specific transferred element $x(\alpha,\beta)$ where $\alpha\in[0,1,\ldots,N-1]$ and $\beta\in[0,1,\ldots,M-1]$ of the matrix $\mathbf{x}$ whose magnitude exceeds the threshold. Hence, for an overall number of elements $\mathcal{R}<NM$ for which magnitudes are over the given threshold, the complexity order is $\left(MN\log_2(M)+\frac{MN}{2}\log_2(N)\right)+O(\mathcal{R})$. Moreover, for SLM-OTFS, a number of candidate phase vector U is generated where each is with dimension of M, i.e., $\mathbf{P}_u=\left[p_{u,0},p_{u,1},\ldots,p_{u,M-1}\right]$ with $u\in[0,1,\ldots,U-1]$, $\mathbf{P}_u$ is a candidate phase vector, and $p_{u,m}\in[-1,1]$. Each u SLM vector is element-by-element multiplied by the corresponding element of each m-row of delay-Doppler matrix. Next, the process of ISFFT and Heisenberg transform are applied. Therefore, the overall SLM-OTFS complexity is U-times equivalent to that of the conventional OTFS, i.e., $\left(UMN\log_2(M)+\frac{UMN}{2}\log_2(N)\right)$. Figure 3 shows a comparison of the CMs computational complexity between the conventional (original) OTFS system (as a reference), the proposed OTFS-based ANN-PAPR reduction scheme, and the OTFS-based SLM-PAPR reduction scheme. From the figure we can observe that the iteration factor results in increased complexity. However, with high value of N the complexity deviation between the original OTFS and the ANN-based OTFS becomes narrow, even with higher iteration factor. On the other hand, the CMs of SLM-OTFS shows a very high difference in complexity compared to the other two systems, especially with the increase in the number of phase vectors U. Lastly, it is important to re-iterate that, with the proposed ANN-PAPR reduction scheme, there is no need for any recovery process at the receiver. As a result, this unique feature of the technique renders the transformation process free from additional computational complexity at the receiver.

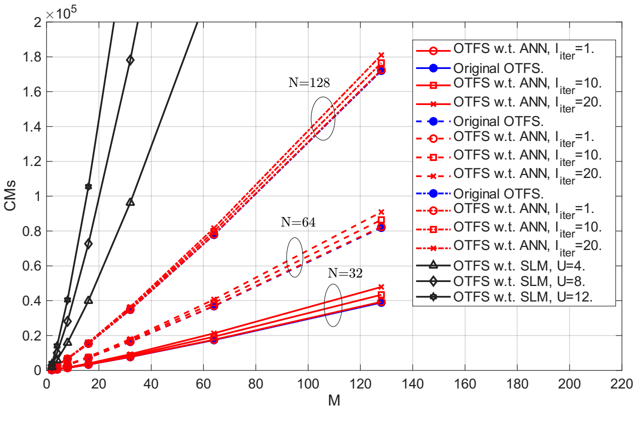

Fig. 3. CMs Computational Complexity of original OTFS, OTFS with the proposed ANN-PAPR reduction and OTFS with the SLM-PAPR reduction at different values of N, $\mathcal{I}_{\mathrm{iter}}$, and U phase vectors.

3. Simulation Results and Discussions

In this section, we present the results of the proposed ANN-PAPR reduction scheme applied to an OTFS system. The simulation code (MATLAB-R2023b) of [15] was modified to include the ANN-PAPR reduction scheme and used in this study. Table 1 lists the parameters used in the simulation. For any pulse shaping waveform, the OTFS signal is considered to be critically sampled, i.e., assuming that $T\Delta f = 1$. Also, a perfect channel state information is assumed, and the channel is supposed to be under-spread, i.e., $\tau_{\max}\nu_{\max} \ll 1$. The assumed channel models are the channel with 4-taps of uniform power (applied with MP detector) and the EVA channel model at user's speed of 500 km/h (applied with MRC detector) [15]. Notice that the obtained CCDF-PAPR simulation results have been referenced to the theoretical curves of the original PAPR of OTFS frame and the SLM-distortionless PAPR reduction technique, which shows the best characterization of PAPR at specific U-phase vectors of OTFS frame.

3.1 CCDF-PAPR Performance

This section provides comparisons of CCDF-PAPR performance with respect to a certain PAPR, in addition to OTFS signal amplitude as a function of time. Besides, more comparisons are presented in Tab. 2. Figure 4 shows the CCDF-PAPR performance of theoretical PAPR for the original OTFS (i.e., without PAPR reduction) and for SLM scheme (with $U = 4$ and 16 candidate phase vectors) and estimated PAPR of the proposed OTFS with the ANN algorithm (ANN-PAPR), in terms of IBO = 5 and 7 dB at different levels of the threshold γ (i.e., at $\epsilon = 0.7, 0.8$ and 0.9) and $N = M = 32$ for the DD matrix. From the figure, we can observe that the the response of the proposed ANN-PAPR scheme is superior to that of the theoretical SLM approach for all levels of threshold when considering both IBOs (5 and 7 dB). In the case of highest levels of threshold (at IBO = 7dB and $\epsilon = 0.9$), the ANN scheme can reduce the PAPR by up to 5.5 dB below the original OTFS-PAPR and the gains by about 3 and 2 dB over the SLM scheme with $U = 4$ and $U = 16$, respectively, at CCDF = 10^{-4}. Notice that some PAPR curves of the ANN scheme did not show any performance after a specific CCDF probability (i.e., does not achieve the CCDF probability level 10^{-4}), which means that the ANN algorithm did not catch further OTFS elements whose magnitudes exceeded the specified CCDF threshold. In other words, the number of elements that exceed a certain CCDF probability

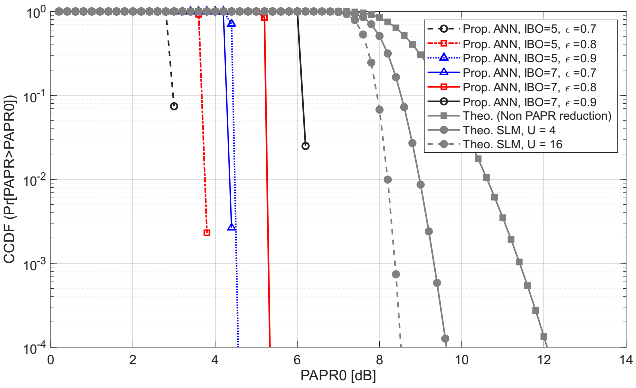

Fig. 4. Comparison of CCDF-PAPR for the proposed ANN-OFTS at different values of IBO [dB] and ϵ with $N = M = 32$, with respect to the theoretical PAPR of SLM and original OTFS (i.e., non-PAPR reduction).

Name	Abbreviation	Value
Number of subcarriers in frequency (delay)	M	32, 64
Number of symbols in time (Doppler)	N	32, 64
Size of QAM constellation	M-QAM	4, 16, 64
Channel model-1	channel with L-taps of uniform power	4-taps
Channel model-2 (delays)	EVA channel model	$[0\ 30\ 150\ 310\ 370\ 710\ 1090\ 1730\ 2510] \times 10^{-9}$
Channel model-2 (pdp)	EVA channel model	$[0\ \ -1.5\ \ -1.4\ \ -3.6\ \ -0.6\ \ -9.1\ \ -7.0\ \ -12.0\ \ -16.9]$
Carrier frequency	f_c [Hz]	4×10^{9}
Subcarrier spacing	Δ_f [Hz]	15000
One time symbol duration in OTFS frame	$T = \frac{1}{\Delta_f}$	$\frac{1}{15000}$
Number of SLM candidate phase vectors (blocks)	U	4, 16
PA input-back-off [dB]	IBO	3–9
Scale factor of threshold level	ϵ	0.1–0.9

Tab. 1. List of parameters used in the simulation process.

CCDF-PAPR	PAPR of prop. ANN (w.o. SLM/PTS) [dB]	PAPR of OTFS-NN [10] [dB]		PAPR of OTFS-PSO [13] [dB]	
		SLM	PTS	SLM	PTS
10^{-3}	$\ll 2.5$ for subcarriers' length of 1024	≈ 8.5 for subcarriers' length of 256	≈ 7.75 for subcarriers' length of 256	≈ 7 for subcarriers' length of 512	≈ 6.5 for subcarriers' length of 512

Tab. 2. CCDF-PAPR comparisons performance between the proposed OTFS-ANN, the prposal of [10], and the proposal of [13].

(P_r [$\mathrm{PAPR}_{\mathrm{ANN}} > \mathrm{PAPR}_0$]) is limited by the use of the ANN scheme. Hence, no further operation is needed by ANN scheme, resulting in no additional computational complexity. Additionally, the ANN scheme can reduce the PAPR even more, however, this could adversely affect the system performance in terms of the bit error rate (BER), as will be explained later. Also, notice that, despite the reasonable level of PAPR reduction achieved by the SLM approach, it introduced very high system computational complexity where the ISFFT operated U (number of SLM candidate phase vectors) times for each element in the DD matrix.

Finally, Figure 5 illustrates the time domain OTFS signal with/without NLPA effect with/without ANN scheme. It demonstrates the effectiveness of the ANN scheme in only adjusting the ISFFT elements whose magnitudes exceed the given threshold ϵ. Hence the original OTFS sample, which was clipped by the NLPA (red dotted line) because it exceeds the saturation level, has been processed by the proposed ANN scheme to produce the modified sample with lower PAPR (black semi-dotted line). On the other hand, samples which were below the threshold, proceed without being processed by the ANN, eliminating any consequential computational complexity.

Even though, no previous study was reported on PAPR reduction of an OTFS-based system using ANN as proposed in this work, simulation results of [10] and [13] are presented in Tab. 2 for comparison purposes. In [10] ANN was combined with SLM/PTS schemes, while in [13] the particle swarm optimization (PSO) algorithm was used with sub-optimal PTS/SLM. Table 2 shows CCDF-PAPR comparisons performance between the proposed ANN-based OTFS, OTFS-NN-SLM/PTS [10], and OTFS-PSO-SLM/PTS [13]. Considering that the number of subcarriers (length of a transmitted frame), mentioned in the table, is the 1D time domain samples vector with length of $NM \times 1$ which is obtained by the row-wise vectorization of the matrix $\mathbf{X}_{\mathrm{tf}}$. Hence, from the table, it can be observed that the CCDF-PAPR of the proposed OTFS-ANN is overcome the others, even though the length of the transmitted frame of the proposed OTFS-ANN is twice as long as the OTFS-NN-SLM/PTS scheme and three times as long as the OTFS-PSO-SLM/PTS. For example, based on the best case of all proposals, at CCDF = 10^{-3}, the proposed OTFS-ANN capables to gain about 9 dB of PAPR reduction from the original OTFS with the frame length of 1024. Whereas, the OTFS-NN-SLM/PTS can reduce PAPR to only $\approx$ 3 dB for NN-SLM and to $\approx$ 3.5 dB for NN-PTS with the frame length of 256, the OTFS-PSO-SLM/PTS can achieve the same gain of the latter with the frame length of 512.

For an additional comparisons of PAPR, a higher size of constellation points and delay-Doppler matrix, namely 64-QAM and $N = M = 64$, have been implemented at different values of IBO in [dB] and threshold level (ϵ) as shown in Tab. 3. As can be observed from the table that, the maximum, mean and hence the PAPR of the original OTFS (without ANN or NLPA) were fixed while the values of the IBO and ϵ were modified. This result is logical, because no factor affect the original OTFS frame. However, in the presence of NLPA and the proposed ANN scheme with reduced values of either IBO or ϵ, further reductions in the maximum, mean and PAPR of ANN-based OTFS system can be obtained. Consequently, the lower the value of IBO or ϵ, the lower will be obtained PAPR. Note that this may inadvertently affect the system BER performance, as will be explained in the next section.

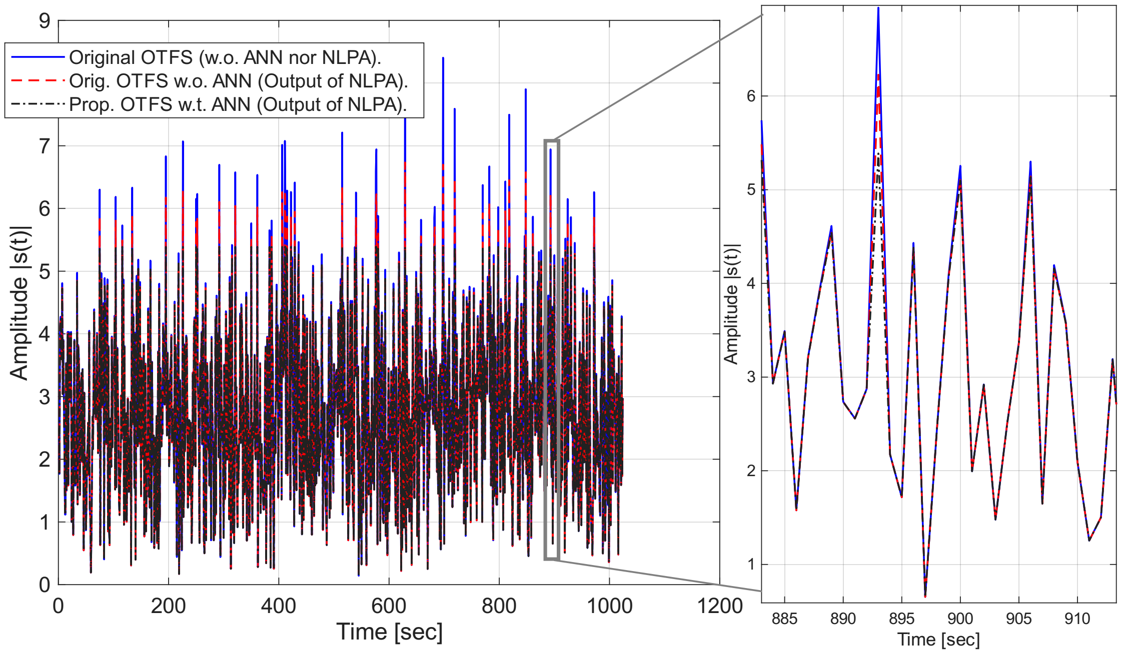

Fig. 5. Comparison of PAPR for time-domain original OTFS (input to the NLPA) and output of NLPA (the OTFS frame with/without ANN) for 16-QAM of $N = M = 32$, IBO = 7 dB and $\epsilon = 0.8$.

64-QAM of OTFS with $N = M = 64$ at different values of IBO [dB] and ϵ	Max. of original OTFS frame (w.o. ANN / NLPA)	Max. of ANN-OTFS frame	Mean. of original OTFS (w.o. ANN / NLPA) frame	Mean. of ANN-OTFS frame	Original OTFS PAPR	ANN-OTFS PAPR
9 and 0.9	17.4908	15.2321	5.7136	5.6915	3.061257351	2.676289203
7 and 0.9	17.4908	12.0663	5.7136	5.6288	3.061257351	2.143671831
5 and 0.9	17.4908	9.4681	5.7136	5.4354	3.061257351	1.741932516
3 and 0.9	17.4908	7.2806	5.7136	5.0065	3.061257351	1.454229502
1 and 0.9	17.4908	5.4106	5.7136	4.2978	3.061257351	1.25892317
9 and 0.7	17.4908	12.4742	5.7136	5.6681	3.061257351	2.200772746
9 and 0.5	17.4908	9.0864	5.7136	5.4447	3.061257351	1.668852278
9 and 0.3	17.4908	5.4537	5.7136	4.3887	3.061257351	1.242668672
9 and 0.1	17.4908	1.8212	5.7136	1.741	3.061257351	1.04606548

Tab. 3. Comparison of CCDF-PAPR for the original OTFS (w.o. ANN) and the proposed ANN-OFTS at different values of IBO [dB] and ϵ with $N = M = 64$ and 64-QAM.

Annotation: The high-power amplifier (HPA) operation within the linear region is adjusted to overcome the non-linearity distortions that occur when amplifying a signal with a non-constant envelope. Either one of the parameters, referred to as Input Back-Off (IBO) or Output Back-Off (OBO), is used to adjust the operational range of the HPA. IBO is defined as the difference between the maximum possible input power and the actual input power, relative to the input power that produces maximum output. While OBO is defined as the difference between the amplifier's maximum possible output power and its actual output power. The core difference between the two parameters is that, IBO is a measure of the input signal's level relative to the point of maximum output, while OBO is a measure of the output signal's level relative to its maximum potential [24], [25]. The IBO parameter has been selected in this study based on the solid-state power amplifier (SSPA) model considered in [21]. Notice that, at very low IBO, say IBO = 0 dB, no output signal is obtained (impractical), while at a very high IBO, say IBO ≥ 10 dB, the effect of the power amplifier is mostly negligible.

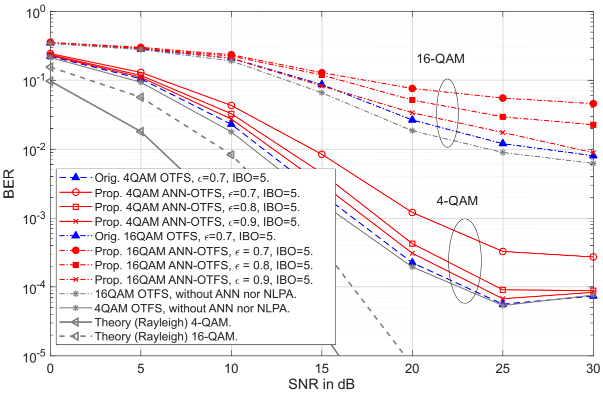

Fig. 6. BER of 4-QAM and 16-QAM for original OTFS frame and the proposed ANN-OTFS frame at variant values of ϵ with $N = M = 32$ and IBO = 5 dB.

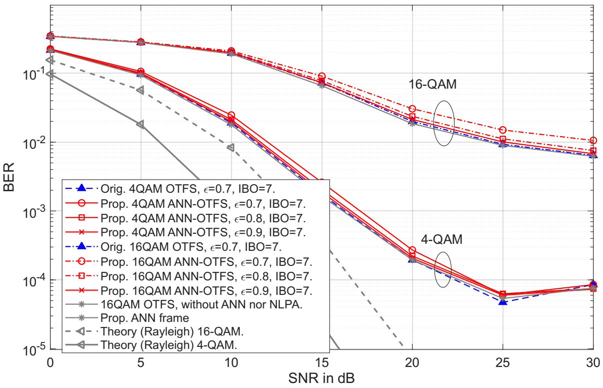

Fig. 7. BER of 4-QAM and 16-QAM for original OTFS frame and the proposed ANN-OTFS frame at variant values of ϵ with $N = M = 32$ and IBO = 7 dB.

3.2 System Performance

This part discusses the system performance (BER) for the modified OTFS based on the proposed ANN scheme at different kinds of detectors, i.e., the MP detector without considering a speed of user, and the Maximum-Ratio combining (MRC) detector with user's speed of 500 km/h. For the MP detector, the BER performance of the proposed ANN-based OTFS is illustrated with $N = M = 32$ at different scaling of threshold level, that is $\epsilon = 0.7, 0.8, 0.9$, for both 4-QAM and 16-QAM at IBO = 5 dB (in Fig. 6) and IBO = 7 dB (in Fig. 7), where both cases refer to the theoretical OTFS performance (i.e., without the effect of the NLPA nor the proposed ANN scheme). These two figures show that the non-linearity level of the NLPA (i.e., the IBO value) affects the overall system performance, regardless of the presence of the PAPR reduction process. For instance, the OTFS system with IBO = 5 dB performs worse than the one with IBO = 7 dB, which means that the linearity of the NLPA has been slightly extended, producing an OTFS signal with a lower distortion. This is further proved by comparing the OTFS system performance, in both figures, at all levels of threshold. It is possible to notice that the system performance (for both 4-QAM and 16-QAM) with IBO = 7 dB for all values of ϵ is superior to that of IBO = 5 dB, which means that the main source of bit errors is the saturation level of the NLPA, and not the threshold levels introduced by the ANN scheme. For the MRC detector, Figure 8 shows the performance of the proposed ANN-OTFS at the user's speed of 500 km/h with $N = M = 32$, $\epsilon = 0.9$, IBO = 7 dB and the modulation of 4-QAM and 16-QAM. The performance of original OTFS and the proposed ANN-OTFS, of MRC detector, is compared with that of MP detector (without a speed of user). In general, it can be observed that, at high SNR, the performance of

MRC is better than that of MP, despite the high user speed, for both modulation sizes 4-QAM and 16-QAM. Notice that, for all scenarios in this figure, the proposed ANN-OTFS performs mostly identical to the original OTFS (i.e., without any PAPR reduction). To conclude, from all BER figures, it can be observed that the ANN-enabled system performs very close to the original OTFS when the threshold is a bit lower than the NLPA saturation level (that is $\epsilon = 0.9$) which is good enough, for both 4-QAM and 16-QAM. This is because, the main aim is to pass the OTFS signal through the NLPA with a magnitude mostly equal to the saturation level. In other words, operating the ANN scheme at a threshold level equivalent to $\epsilon = 0.9$ of the NLPA saturation level satisfies both the PAPR reduction and BER performance levels. This is addition to the distinct feature of the proposed ANN-scheme of not requiring a recovery process at the receiver, resulting in a lower computational complexity compared to conventional PAPR reduction techniques.

Annotation: it is noticed that some BER curves show rising at their tails (i.e., at high SNR). The likely reason behind this situation is the high number of simulation iterations, which is typically $> 1,000,000$ iterations. With this in mind, each simulation per BER cure will take very long time, especially with high sizes of delay-Doppler matrices. Therefore, a lower number of iterations has been considered for these simulation results, with focus on the convergence/divergence between the BER performance of original OTFS and that of the proposed ANN-based OTFS. Otherwise, this increase in BER after SNR = 25 dB could also be attributed to errors, probably, produced from the effect of NLPA, channel, or the detector itself. It is worth mentioning that the ANN operation does contribute to this problem as the increase in BER even happened with the original OTFS signal which did not include the ANN process.

Last but not lease, Figures 9 and 10 illustrate the BER performance for higher size of delay-Doppler matrix and order of constellation mapping, that is $N = M = 64$ and 64-QAM respectively, at variant values of IBO (in Fig. 9) and ϵ (in Fig. 10), considering the MRC detector with user's speed of 500 Km/h. As can be noticed from these figures, the lower values of IBO or ϵ the worse BER performance is introduced. For instance, at IBO = 3 in Fig. 9, the BER of both the original OTFS and ANN-OTFS are perform badly, even with high value of the threshold (at $\epsilon = 0.9$). This is because of the considered low IBO value of the power amplifier. However, it can be noticed that the performance of the proposed ANN-based OTFS is not too far, in somehow, from the original OTFS. This gap is due to the additional cut which is produced by the threshold of ANN itself, that is at $\epsilon = 0.9$ which means 10% below the original signal peak is removed in addition to the clipping of the considered IBO. Moreover, at IBO = 9 dB, the BER of original OTFS and the proposed ANN-based OTFS are identical. This analysis is confirmed in Fig. 10 when the performance of the proposed ANN-based OTFS become worse when reducing further the threshold level ϵ even though the IBO is high, namely at IBO = 9 dB, because the lower threshold means nothing but higher clipping level which produces a significant distorted signal out of the ANN scheme. In general, from all BER figures (Figs. 6–10), the BER performance of OTFS system (with/without the proposed ANN scheme) becomes worse with increasing the size of constellation points, i.e., from 4-QAM to 64-QAM. This suggests that the likely reason behind this result is the channel effects and, probably, due to the inter-modulation-interference and detectors' errors.

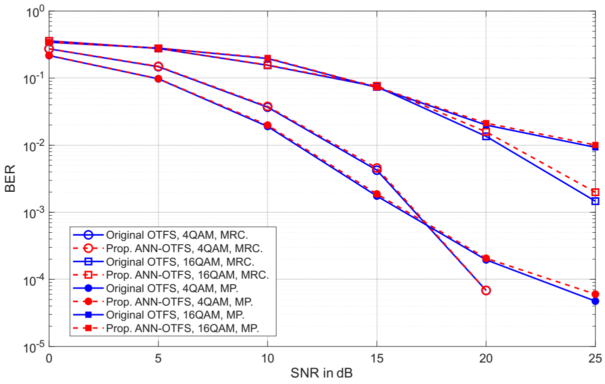

Fig. 8. BER of 4-QAM and 16-QAM for original OTFS frame and the proposed ANN-OTFS frame using MP and MRC (at speed of 500 km/h) detectors, $\epsilon = 0.9$, $N = M = 32$ and IBO = 7 dB.

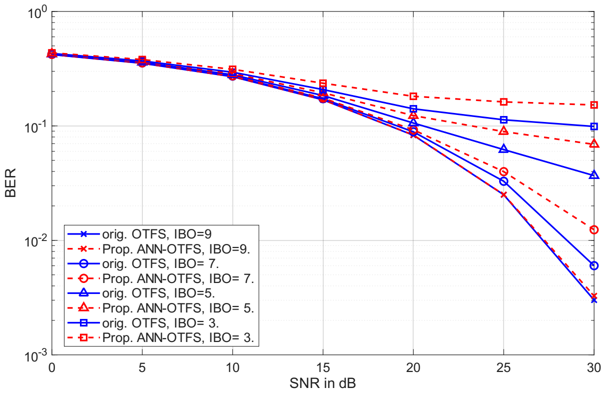

Fig. 9. BER of 64-QAM OTFS for original frame comparing to the ANN-OTFS performance at different values of IBO [dB] using MRC detector (at user's speed of 500 km/h) with $\epsilon = 0.9$, $N = M = 64$.

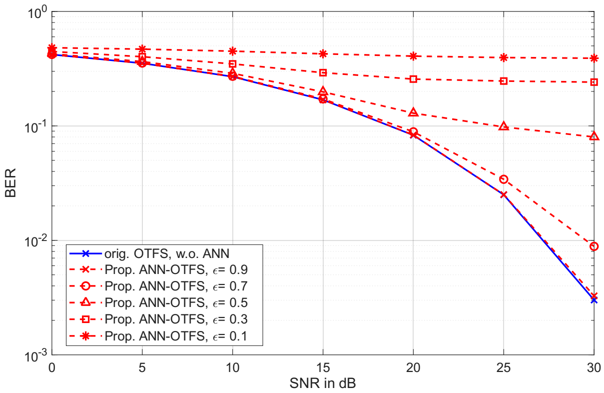

Fig. 10. BER of 64-QAM OTFS for original frame comparing to the ANN-OTFS performance at different values of ϵ using MRC detector (at user's speed of 500 km/h) with IBO = 9 dB, $N = M = 64$.

4. Conclusion

In this work, a simple, yet effective artificial neural network-based PAPR reduction method was proposed which also achieved reasonable levels of system BER performance and lower computational complexity. The proposed ANN-PAPR reduction scheme was operated only to reduce the magnitude of any ISFFT sample element which exceeded the specified threshold level $\gamma = \epsilon A_0$. In fact satisfactory levels of PAPR reduction and BER performance were achieved with an ANN threshold level of up to $\epsilon = 0.9$ which favourably compares to the theoretical results. In addition, the proposed scheme does not require a recovery process at the receiver which further lower the computational complexity, unlike conventional PAPR reduction techniques. Moreover, the proposed ANN-PAPR technique can be recommended as a reasonable solution for reducing the PAPR of any multicarrier communication system including 5G/6G systems.

Acknowledgments

This research was funded by the Ongoing Research Funding program, (ORF-2025-484), King Saud University, Riyadh, Saudi Arabia.

References

[1] CAI, D., FANG, F., LI, Q., et al. Secure precoding design for high-mobility systems with OTFS modulation. *Physical Communication*, 2023, vol. 61, p. 1–8. DOI: 10.1016/j.phycom.2023.102179

[2] SHARMA, S., HAIDER-SHAH, S., WIDMER, J. A low-complexity standard-compliant PAPR reduction scheme for OTFS modulation. In *Proceedings of the 99th Vehicular Technology Conference (VTC2024-Spring)*. Singapore, 2024, p. 1–7. DOI: 10.1109/VTC2024-Spring62846.2024.10683635

[3] ELDUKRI, E. E., AL-RAYIF, M. I. A conditionally applied neural network algorithm for PAPR reduction without the use of a recovery process. *ETRI Journal*, 2024, vol. 46, p. 227–237. DOI: 10.4218/etrij.2022-0470

[4] CHENNAMESETTY, S., BODDU, S., CHANDHAR, P., et al. Analysis of PAPR in OTFS modulation with classical selected mapping technique. In *Proceedings of the 15th International Conference on Communication Systems and Networks (COMSNETS)*. Bangalore (India), 2023, p. 319–322. DOI: 10.1109/COMSNETS56262.2023.10041313

[5] KUMAR, A., SHARMA, H., GAUR, N., et al. PAPR analysis in OTFS using the centre phase sequence matrix based PTS method. *Results in Optics*, 2024, vol. 15, p. 1–8. DOI: 10.1016/j.rio.2024.100664

[6] GAO, S., ZHENG, J. Peak-to-average power ratio reduction in pilot-embedded OTFS modulation through iterative clipping and filtering. *IEEE Communications Letters*, 2020, vol. 24, no. 9, p. 2055–2059. DOI: 10.1109/LCOMM.2020.2993036

[7] ZHOU, D., WANG, S., ZHENG, Z., et al. A cross-domain PAPR reduction method for OTFS modulation. In *Proceedings of the IEEE/CIC International Conference on Communications in China (ICCC)*. Hangzhou (China), 2024, p. 2089–2094. DOI: 10.1109/ICCC62479.2024.10681770

[8] SU, J., LIU, S., HUANG, Y., et al. Peak-to-average power ratio reduction via symbol precoding in OTFS modulation. In *Proceedings of the 95th Vehicular Technology Conference (VTC2022-Spring)*. Helsinki (Finland), 2022, p. 1–5. DOI: 10.1109/VTC2022-Spring54318.2022.9860629

[9] XIONG, J., ZHU, J., DU, J., et al. An expanded precoding scheme for PAPR reduction in OTFS modulation. In *Proceedings of the IEEE Wireless Communications and Networking Conference (WCNC)*. Dubai (United Arab Emirates), 2024, p. 1–5. DOI: 10.1109/WCNC57260.2024.10571084

[10] KUMAR, A., GAUR, N., ALY, A. A., et al. PAPR reduction of OTFS using an automatic amplitude reduction neural network with Vandermonde matrix-based PTS and SLM algorithms. *EURASIP Journal on Wireless Communications and Networking*, 2024, vol. 2024, p. 1–18. DOI: 10.1186/s13638-024-02414-z

[11] ABDULLAH, E., DIMYATI, K., MUHAMAD, W. W., et al. Deep learning based asymmetrical autoencoder for PAPR reduction of CP-OFDM systems. *Engineering Science and Technology, an International Journal*, 2024, vol. 50, p. 1–12. DOI: 10.1016/j.jestch.2023.101608

[12] LIU, M., ZHAO, M., LEI, M., et al. Autoencoder based PAPR reduction for OTFS modulation. In *Proceedings of the 94th Vehicular Technology Conference (VTC2021-Fall)*. Norman (USA), 2021, p. 1–5. DOI: 10.1109/VTC2021-Fall52928.2021.9625251

[13] ALANAZI, M. H., KUMAR, A., ALJEBREEN, M., et al. Reducing PAPR in OTFS 6G waveforms using particle swarm optimization-based PTS and SLM techniques with 64, 256, and 512 sub-carriers in Rician and Rayleigh channels. *Fractals*, 2024, vol. 32, no. 9–10, p. 1–16. DOI: 10.1142/S0218348X25400183

[14] AL-RAYIF, M. I. PAPR reduction of OTSM with random and orthogonal SLM phase sequences and its recovery in the presence of EPA, EVA, and ETU channel models. *Radioengineering*, 2024, vol. 33, no. 4, p. 744–757. DOI: 10.13164/re.2024.0744

[15] HONG, Y., THAJ, T., VITERBO, E. *Delay-Doppler Communications Principles and Applications*. 1st ed. London (UK): Academic Press, 2022. ISBN: 978-0-323-85028-5

[16] MOHAMMED, S. K. Derivation of OTFS modulation from first principles. *IEEE Transactions on Vehicular Technology*, 2021, vol. 70, no. 8, p. 7619–7636. DOI: 10.1109/TVT.2021.3069913

[17] THAJ, T., VITERBO, E. Low complexity iterative Rake decision feedback equalizer for zero-padded OTFS systems. *IEEE Transactions on Vehicular Technology*, 2020, vol. 69, no. 12, p. 15606–15622. DOI: 10.1109/TVT.2020.3044276

[18] RAVITEJA, P., HONG, Y., VITERBO, E., et al. Practical pulse-shaping waveforms for reduced-cyclic-prefix OTFS. *IEEE Transactions on Vehicular Technology*, 2019, vol. 68, no. 1, p. 957–961. DOI: 10.1109/TVT.2018.2878891

[19] RUMELHART, D. E., DURBIN, R., GOLDEN, R., et al. *Backpropagation: Theory, Architectures, and Applications*. 1st ed. New York (USA): Psychology Press, 1995. DOI: 10.4324/9780203763247

[20] SURABHI, G. D., AUGUSTINE, R. M., CHOCKALINGAM, A. Peak-to-average power ratio of OTFS modulation. *IEEE Communications Letters*, 2019, vol. 23, no. 6, p. 999–1002. DOI: 10.1109/LCOMM.2019.2914042

[21] DUDAK, C., KOC, A. T., KOC, S. Solid-state power amplifier (SSPA) nonlinearity effects on quadrature phase shift keying modulation. In *Proceedings of the 7th European Conference on Wireless Technology*. Amsterdam (Netherlands), 2004, p. 237–240. ISBN: 1-58053-991-2

[22] STRAUSS, R. Reliability of SSPAs and TWTAs. *IEEE Transactions on Electron Devices*, 1994, vol. 41, no. 4, p. 625–626. DOI: 10.1109/16.278524

[23] FARHANG, A., REZAZADEHREYHANI, A., DOYLE, L. E., et al. Low complexity modem structure for OFDM-based orthogonal time frequency space modulation. *IEEE Wireless Communications Letters*, 2018, vol. 7, no. 3, p. 344–347. DOI: 10.1109/LWC.2017.2776942

[24] CHRISTOPH, R. Effects of HPA nonlinearity on 4-DPSK/OFDM signal for a digital sound broadcasting system. In *Proceedings of the 2nd European Conference on Satellite Communication*. Liege (Belgium), 1991, p. 179–184.

[25] LIANG, C., JONG, J., STARK, W., et al. Nonlinear amplifier effects in communication systems. *IEEE Transactions on Microwave Theory and Techniques*, 1999, vol. 47, no. 8, p. 1461–1466. DOI: 10.1109/22.780395

About the Authors ...

Mohammed AL-RAYIF holds a bachelor's degree in Electrical Engineering from King Saud University, Riyadh, Saudi Arabia. He received his MSc and PhD degrees from Newcastle University, UK in 2006 and 2010 respectively in Communications and Signal Processing. From 1998 to 2014, he held several positions in the General Directorate of Border Guards in the Ministry of Interior in the Kingdom of Saudi Arabia, including for example the Head of Wired / Wireless Systems Department (2000–2003) and Director of Communications Systems in the Border Guards (2011–2013). He served as Chairman of the Electrical Engineering Department and Vice Dean of the College of Engineering at King Khalid University in Ahab (2014–2017). During the period 2018–2019, he was a collaborating faculty member with the Department of Applied Electrical Engineering, Al-Muzahimiyah branch, King Saud University. Mohamed Al-Rayif has been working since 2019 as an associate professor in the Department of Applied Electrical Engineering. His research interests include OFDM and MIMO systems, artificial intelligence techniques, mm wave communications, OTFS and OTSM systems. Mohammed Al-Rayif has contributed his research publications to many prestigious international journals and conferences.

Eldaw E. ELDUKHRI is an Associate Professor at the College of Applied Engineering, King Saud, University, Kingdom of Saudi Arabia since 2016. He obtained his BEng (Electrical) degree with First-class Honours from Sudan University of Science and Technology, Khartoum, Sudan in 1988. He received his MSc and PhD degrees from Salford University, United Kingdom in 1992 and 1996 respectively. From 1999 to 2016, he was Senior Research Fellow/Senior Lecturer at Cardiff School of Engineering, Cardiff University, UK. Between 1996 and 1999, he was Assistant Professor and Head of Electrical Engineering Department, Sudan University of Science and Technology, Sudan. In the period 2004 to 2009, he was the manager of the EU Network of Excellence on Innovative Production Machines and Systems (I*PROMS) which comprised 30 partner organizations from 14 European countries including universities, research centers and multinational companies. He was also the Chair of the Organizing Committee for the Virtual International Conference series organized by the Network and co-editor of the Conference Proceedings and consequent special issues in relevant international journals. He organized and chaired many special sessions within international conferences and published numerous conference and journal papers. He is Chartered Engineer (CEng) and member of both the Institution of Engineering and Technology (IET) and the Institute of Electrical and Electronics Engineers (IEEE). His research interests include: control systems design and applications, advanced robotics, mechatronics, applications of AI.